Published in final edited form as:
Nat Commun. ; 1: 41. doi:10.1038/ncomms1042.

Multifunctional nanoparticles as coupled contrast agents

Yongdong Jin[1], **Congxian Jia**[2], **Sheng-Wen Huang**[1], **Matthew O'Donnell**[1,2], and **Xiaohu Gao**[1]

[1]Department of Bioengineering, University of Washington, William H Foege Building N530M, Seattle, WA 98195, USA

[2]Department of Biomedical Engineering, University of Michigan, Ann Arbor, MI 48109, USA

Abstract

Engineering compact imaging probes with highly integrated modalities is a key focus in bionanotechnology and will have profound impact on molecular diagnostics, imaging, and therapeutics. However, combining multiple components on a nanometer scale to create new imaging modalities unavailable from individual components has proven challenging. Here, we demonstrate iron oxide and gold coupled core-shell nanoparticles with well defined structural characteristics (*e.g.*, size, shell thickness, and core-shell separation) and physical properties (*e.g.*, electronic, magnetic, optical, thermal, and acoustic). The resulting multifunctional nanoprobes not only offer contrast for electron microscopy, magnetic resonance imaging, and scattering-based imaging, but more importantly, enable a *new* imaging mode, magnetomotive photoacoustic (mmPA) imaging, with remarkable contrast enhancement compared to PA images using conventional nanoparticle contrast agents.

The development of multifunctional nanoprobes enabling new imaging modalities beyond the intrinsic limitations of individual components is of considerable interest to many research areas, ranging from fundamental biology to molecular imaging and medical diagnostics. Recent advances in nanotechnology have produced a variety of nanoparticle probes such as semiconductor quantum dots (QDs), magnetic nanoparticles (MNPs), and metallic NPs. Their unique electronic, magnetic, optical, and structural properties have addressed a broad spectrum of biomedical applications, such as ultrasensitive detection, medical imaging, and targeted therapeutics.[1–3] Similar to conventional small molecule-based imaging probes, however, each type of nanoprobe displays distinct advantages as well as limitations.[4, 5] For example, MNPs have become an important contrast agent in T2-weighted magnetic resonance imaging (MRI) because MRI offers high-resolution and excellent tissue penetration depth. On the other hand, MRI is not as sensitive as optical imaging or positron emission tomography, and is difficult to visualize in microscopic tissue examination.[6] Similarly, gold NPs are often used in scattering based imaging and offer high sensitivity, high resolution, and multiplexing capability.[7] But the tissue penetration depth of optical imaging is limited to millimeters.[6] Therefore, a major challenge is how to engineer molecular probes with integrated functionalities while still maintaining compact sizes.[8]

Correspondence and requests for materials should be addressed to M.O.D. (odonnel@u.washington.edu) and X.H.G. (xgao@u.washington.edu).

Author Contributions

Y.J., X.H.G., M.O.D. conceived the idea and designed the project. Y.J., S.W.H., and C.J. carried out the experiments. Y.J., C.J., S.W.H., M.O.D., and X.H.G. analyzed the data. Y.J., X.H.G., C.J.S., S.W.H., and M.O.D. wrote the manuscript.

Additional information

Supplementary Information accompanies this paper on www.nature.com/naturecommunications.

Competing financial interests: Authors declare they have no competing financial interests.

Furthermore, it is highly desirable that nanoprobes with coupled functionalities will enable new imaging modes not available from each individual component for enhanced contrast specificity.

A long sought-after coupled imaging probe is noble metal, such as Pt and gold, coated MNPs,[9, 10] with precisely controlled shell thickness and smooth surface, due to a number of desirable properties including magnetic attraction, near-infrared (NIR) absorption, photon scattering, and easy biomolecular conjugation through the stable thiolate-gold interaction. Several attempts have been made by directly coating gold onto MNPs[11–18] or MNP-silica composites (utilizing the low dielectric permittivity of silica).[19–21] However, neither approach *simultaneously* produces NPs with NIR response (critical for *in vivo* imaging and therapy) and yet maintains compact particle size (affects tissue penetration and plasma circulation). For example, gold coating on MNP-silica composites often results in large particles of 100–200 nm in diameter with uneven surfaces.[19–21] Similarly, direct coating of gold onto iron oxide NPs requires both a large core particle and thick gold coating for NIR response.[12–14] This is because, in contrast to silica-gold core-shell NPs whose absorption profile red-shifts with decreasing shell thickness, iron oxide-gold core shell particles absorb at longer wavelengths with increasing shell thickness.[13] As a consequence, compact MNPs with thin gold coating only absorb in the visible spectrum.[17, 18] For NIR response, MNP-gold core-shell particles must be large in overall size (100–400 nm).[12–14]

Here, we report a new generation of compact, uniform, NIR responsive MNP-gold core-shell nanostructures by creating a gap between the core and shell. Not only does this approach produce a magnetically sensitive NP with both strong NIR and MR responses, it also enables a new modality, magnetomotive photoacoustic (mmPA) imaging. Compared to PA imaging using conventional metallic NPs, mmPA imaging with a coupled agent provides the same sensitivity but with markedly improved contrast specificity. Indeed, all PA signals not created by the coupled NP potentially can be suppressed to the electronic noise limit of the imaging system.

Results

Synthesis of MNP-gold core-shell nanoparticles

Figure 1 schematically illustrates the major steps in making the MNP-gold coupled NPs and how they can be used for mmPA imaging. Highly monodisperse MNPs with hydrophobic surface ligands, oleic acid, are first solubilized into aqueous solution using phospholipid-polyethylene glycol terminated with carboxylic acid (PL-PEG-COOH). The hydrophobic PL segment interdigitates with oleic acids through hydrophobic interactions, whereas the PEG block facing outward renders the MNPs water-soluble and negatively charged due to the terminal carboxylic acids. To create anchor points for gold shell growth, a layer of positively charged peptide, poly-L-histidine (PLH), is adsorbed onto the outer surface of MNP-PEG via charge-charge interaction at pH 5–6. Indeed, zeta potentials of the PEG solubilized MNPs before and after coating with PLH were –15.5 and +9.1 mV, respectively. This surface charge inversion suggests a successful layer-by-layer surface coating of polyelectrolytes (ionic polymers) on the NP surfaces.

Previously, we have synthesized quantum dot-gold core-shell particles using similar approaches and shown that in contrast to commonly used primary amines, the imidazole groups in PLH are capable of immobilizing Au^{3+} ions on QD surfaces at high packing density.[22] This is perhaps not surprising since metal ion chelating by histidine-containing peptides has been studied extensively for affinity chromatography. The multilayer organic molecules coated on the MNP surface (oleic acid, PL-PEG, and PLH) act as an effective barrier preventing gold ions from direct growth on the iron oxide core. Further reduction of

Au^{3+} with a reducing reagent leads to the formation of multifunctional MNP-gold core-shell particles with clear separation and only small size increase over the original MNPs. In contrast to the QD-gold hybrid which does not offer new imaging mechanisms,[22] the resulting coupled MNP-gold nanoprobe provides contrast not only for conventional modalities such as TEM, optical imaging, PA imaging, MRI, but also for the new modality of mmPA imaging.

Principle of mmPA imaging

Figure 1b illustrates how MNP-gold NPs can be manipulated for mmPA imaging. During real-time PA data acquisition, a pulsed magnetic field is applied. Voxels within the imaging region experience a force induced by the local field and magnetization. When the field is on, MNP-gold NPs move as a result of their strong magnetization, creating a moving source within a PA image. When the field is turned off, MNP-gold NPs return to their original positions. Non-magnetic PA sources do not move coherently with the applied field during this entire interval. Consequently, coherent motion processing of a PA image sequence (Fig. 1c) can identify sources related to MNP-gold NPs and reject all background signals whether from diffuse or localized sources. Such processing can greatly enhance the contrast specificity of the NP. By comparison, bare MNPs are not a suitable contrast agent for PA or mmPA imaging even though they can respond to magnetic field. Bare MNPs do not absorb efficiently in the NIR and, consequently, exhibit poor PA efficiency. Similarly, although plasmonic nanomaterials, such as Au nanorods, have large NIR absorption per particle and high PA efficiency, their signals could be buried by high backgrounds often seen in optical and acoustic imaging.

Characterization of MNP-gold coupled contrast agents

Although the engineering of MNP-gold NPs applies to MNPs of various sizes (Supplementary Figure S1), the synthesis, characterization, and applications of the coupled nanoprobe discussed below are focused on one representative MNP with a 25 nm diameter (Fig. 2a). TEM images show MNP-gold core-shell NPs with different shell thickness and a gap of ca. 3 nm between core and shell due to the low electron density of the embedded organic molecules. In contrast to conventional approaches in which only thick gold nanoshells can be coated onto NPs,[23] PLH templated gold deposition can be controlled with nanometer precision to form an ultrathin and relatively smooth shell layer.[22] As a result, a gold nanoshell less than 3–4 nm thick enabled direct observation of the internal structure of the MNP-gold core-shell NPs (Fig. 2b&c). When the shell thickness was slightly increased to 4–5 nm, the core-shell internal structure disappeared and manifested as solid dark dots (Fig. 2d). Note that the 4–5 nm shell thickness was not directly measured (not visible under TEM), but was derived from the overall particle size increase compared with original MNPs and MNPs coated with thin gold layers (Fig. 2e–h).

Given that TEM imaging under inappropriate focusing conditions could possibly show blurred ring structures around NPs, high resolution TEM (HR-TEM) was also performed to ensure that the core–shell structure observed was not an imaging artifact. Two representative images are show in Fig. 2 i&j. Despite their relatively low contrast compared to low-magnification images on ultrathin nanomaterials,[24] the signature crystal lattices of iron oxide and gold are clearly visible, which unambiguously confirms the core-shell structure. We also noted that due to the ultrathin nature, it would be difficult to achieve a completely uniform gold shell without gaps or pores. Prior research has shown that although gold shells impart remarkable resistance to oxidation and acid-etching for embedded iron oxide NPs, a relatively thick Au layer is needed to completely isolate the core particle from the environment.[11, 25] Further improvements of the evenness of the thin shells could be made

via new nanocrystal synthesis techniques such as nonepitaxial shell growth.[26] Nevertheless, for this paper, the most desirable property is not a poreless shell, but strong NIR absorption.

Next, we thoroughly characterized the optical and magnetic properties of the hybrid nanoparticles as well as their stability against NIR laser irradiation. The core-shell NPs display shell-type NIR absorption.[23] Figure 3a shows the extinction spectra of MNP-gold core-shell hybrid particles corresponding to the TEM images shown in Fig. 2a–d. In comparison to MNPs successively coated with PL-PEG-COOH and PLH polymer layers exhibiting negligible NIR absorption, the surface plasmon resonance (SPR) band appeared in the NIR spectrum with formation of thin gold nanoshells. The SPR peaks of the core shell structures are significantly enhanced (intensity well above that of the original MNP core), which is desirable for photoacoustic imaging. Note that the elevated curves are part of the extinction signals instead of noise, which is commonly seen in shell-type plasmonic materials.[23] For 1–2 nm thick gold shells, the SPR band centered around 900 nm. As the thickness increased to 2–3 nm and 4–5 nm, SPR extinction peak blue-shifted to 760 nm and 660 nm, respectively, following a similar trend to that of silica-gold nanoshells.[23] This spectroscopic measurement confirms the electron microscopy results of Fig. 2 showing that the gold shell is separated from the iron oxide core (red-shift in the visible spectrum with increasing shell thickness would be expected otherwise[13]). We also noticed that the extinction peaks of hybrid NPs are broader than theoretical values. This kind of line broadening is commonly seen in virtually all gold shell nanostructures,[13, 14, 17, 27, 28] and has been attributed to the combination of a number of factors including phase retardation effects, size distribution of both cores and shells, and electron scattering at the shell interfaces.[29]

The magnetization of the hybrid NPs (2–3 nm gold shell) was measured using superconducting quantum interference device (SQUID) magnetometry. The temperature dependence of the zero-field-cooled/field-cooled (ZFC/FC) magnetization is shown in Supplementary Figure S2. The two curves overlap at high temperature and quickly depart from each other as the temperature decreases. The ZFC curves show maxima at 275 K and 270 K (blocking temperature, T_b) for MNPs before and after coating with thin Au shells, which is characteristic behavior of superparamagnetism.[9, 20] The T_bs of MNPs are well below room temperature and the slight decrease after surface coating has been previously observed as well. It is believed to reflect the decreased coupling of the magnetic moments as a result of the increased interparticle spacing of magnetic cores,[18] which is due to a combination of the Au and the polymer capping shells for the hybrid NPs. For superparamagnetic colloids, the *M-H* curve should not show hysteresis when measured above T_b. Indeed, no hysteresis was detected at room temperature after MNPs were coated with a thin gold shell and the saturation magnetization of the magnetic cores was only reduced slightly (Fig. 3b). The compact core-shell NPs do not aggregate in solution, but respond magnetically. When an external magnetic field was applied, the NPs were slowly isolated by the magnetic force (> 3h). The remaining liquid became colorless, indicating that the plasmonic response was indeed due to gold nanoshells on MNPs instead of self-nucleated gold NPs (Fig. 3b **inset**).

Besides the optical and magnetic properties, we further characterized particle stability under NIR laser irradiation, since the biomedical applicability of this technology strongly depends on probe stability. For example, one of the most common uses of plasmonic nanomaterials is photothermal therapy, where electromagnetic radiation is converted into heat to treat diseased cells.[7, 30] Therefore, the nanoprobe stability is directly linked with the therapeutic effects. Compared with two popular goldbased NIR-responsive nanoprobes, nanorods and nanocages,[31–35] both of which have been used in imaging and therapy, the MNP-gold core-shell NPs exhibited remarkable stability under identical laser irradiation. As shown in Fig.

3c, both gold nanorods and nanocages were stable at laser fluences below 2 and 6 mJ/cm^2, respectively. Above these fluences, significant SPR peak shifts were observed indicating nanoprobe degradation. In contrast, only slight peak shifts were observed for the MNP-gold hybrid NPs when the laser fluence was increased to 10–15 mJ/cm^2. Significant spectral shifts were also observed when the laser fluence was further increased.

Multimodality imaging using coupled contrast agents

To demonstrate the use of this technology for multimodality imaging, we first tested the MNP-gold hybrid NPs with conventional modalities, including dark field, PA, and MR imaging. In addition to the EM images shown in Fig. 2 based on the high electron density of both core and shell materials, MNP and gold have highly complementary features for other imaging modes. As shown in Fig. 4a&b, the strong scattering property of gold nanoshell makes the hybrid NPs an excellent optical imaging probe. Samples of dilute uncoated and gold shell encapsulated MNPs were spread on glass coverslips, resulting in spatially isolated single NPs on the surface. Under dark field imaging conditions, the MNP-gold hybrid NPs are easily detectable but not the original MNPs. On the other hand, scattering-based imaging does not allow deep tissue imaging, but MRI does. To demonstrate the MRI capability of these hybrid particles, we compared them to conventional MNPs. Serial dilutions of MNPs with and without the gold nanoshell coating exhibited nearly identical image contrast (Fig. 4c), which confirmed the SQUID results that the MNPs maintained their magnetic properties after coating with thin gold shells.

Besides scattering, the second feature unique to the gold nanoshell is the strong NIR absorption, and companion energy release in the form of heat, which can be utilized for photothermal therapy[36] and PA imaging.[37, 38] Compared with the shallow photon penetration depth of scattering techniques, PA imaging can sample optical phenomena within tissue to a depth of several cm.[39] It is also significantly cheaper to operate and more portable than MRI. Absorption of pulsed NIR laser light creates acoustic sources within tissue, where the source strength is proportional to the local absorption of the optical pulse. An image is formed using conventional ultrasound technology, where PA contrast is directly related to optical absorption.

To test the efficacy of MNP-gold particles as PA contrast agents, water solutions consisting of no particle, 5 nM MNPs, and 5 nM MNP-gold hybrid NPs were injected sequentially into a polycarbonate tube and illuminated with a 750 nm pulsed laser. Figure 4d&e shows cross-sectional PA images of the tube corresponding to the different solutions on a decibel (dB) scale, with 0 dB corresponding to the maximum signal level across all images. Compared to the MNP solution, MNP-gold of the same concentration improved image signal-to-noise ratio by nearly 1 order of magnitude (i.e., 20 dB) due to the strong gold-shell SPR absorption.

mmPA using MNP-gold coupled contrast agents

Next we demonstrated that MNP-gold hybrid NPs' strong magnetization and NIR absorption enable mmPA imaging with significantly improved contrast specificity compared with conventional PA imaging. A 3-mm thick, 10% polyvinyl alcohol (PVA) disk was constructed as an imaging phantom. It contained three 2-mm diameter cylindrical inclusions made of 10% PVA mixed with 8% 15-um polymer beads. The first, containing gold nanorods with comparable absorption coefficient as 3 nM MNP-gold hybrid NPs, serves as a magnetic reference, i.e., a localized "background" region to be suppressed in mmPA imaging. The second, containing 3 nM MNP-gold hybrid NPs, serves as an object of interest. And the third, containing 3 nM MNPs, serves as an optical reference. An electromagnet generating 5-s 0.7-Tesla pulses was placed under a water tank holding the

phantom. Figure 5a shows a cross-sectional PA image on a dB scale of the PVA phantom at 720 nm optical wavelength with 0 dB corresponding to the maximum signal level across all images. The inclusion with MNP-gold hybrid NPs (middle) is one order of magnitude (i.e., 20 dB) brighter than the one with MNPs (right), in agreement with Fig. 3a. While the inclusion with gold nanorods (left) has comparable PA strength to that with MNP-gold hybrid NPs, it is suppressed in the mmPA image shown in Fig. 5g.

An mmPA image can be derived from a series of PA images in a variety of ways. Figure 5 illustrates the current signal processing scheme. A conventional PA image (Fig. 5a) sequence was acquired in synchrony with a magnetic pulse. The displacement of each pixel in a PA image from its initial position was tracked using a conventional speckle tracking algorithm[40] over the entire 10 second interval, with the magnetic pulse spanning the first 5 seconds. Figure 5b shows the maximum displacement at the end of the magnetic pulse. For each pixel, we fitted the displacement as linear functions of time over the two 5-second intervals when the field was on/off. A pixel with positive slope in the first half and negative slope in the second half was subsequently fitted to two cascaded exponential functions using nonlinear least squares curve fitting. Three representative fitted curves are shown in Fig. 5c for three pixels within the inclusions. Using these curves at every pixel, the velocity was computed over the full 10-second interval (Supplementary Movie S1), and the maximum positive and negative velocities, shown in Fig. 5d&e, were used to create a weighting image (Fig. 5f) based on the magnitude of the difference between the peak positive velocity in the first half and the peak negative velocity in the second half. Fig. 5g shows the mmPA image produced from the product of Fig. 5a and Fig. 5f, where the gold nanorod inclusion is almost completely suppressed.

Discussion

Although the principle of suppressing strong PA sources not susceptible to an applied magnetic field (e.g., the gold nanorod inclusion above) in mmPA imaging has been demonstrated, finite background motion in real clinical imaging from physiological sources such as cardiac motion and respiration can interfere with induced motion. Other imaging modalities, such as acoustic radiation force impulse (ARFI) imaging and thermal strain imaging (TSI), have a similar problem of tracking small induced displacements during physiologic motion. Robust signal processing methods have been developed to track induced motion by synchronizing the data acquisition sequence with physiologic motion.[41, 42] Similar methods can be developed for clinical applications of mmPA imaging.[43] We also note that motion filtering may not need to be performed for all PA imaging for contrast enhancement, but high background is commonly seen in PA imaging similar to optical imaging and MRI.

In mmPA imaging, the induced motion depends not only on the magnetic field but also on tissue elastic properties. Therefore, in biomedical applications, it is hard to quantitate the contrast agent concentration based on motion alone. For example, displacements and velocities in the MNP inclusion were slightly greater than those in the MNP-gold hybrid NP inclusion primarily because of differences in the elasticity of the inclusions (Supplementary Figure S3). However, the induced motion, regardless of scale, is coherent with the applied magnetic field. By detecting motion in response to a time-varying magnetic field, contrast can be greatly improved. The ability to enhance regions with targeted contrast agents makes mmPA imaging an attractive modality for molecular diagnostics. In addition, because the displacement time course depends on tissue elastic properties (e.g., after the magnetic field is turned off, displaced tissue moves back to its original position subject only to intrinsic elastic properties such as relaxation), mmPA imaging can potentially also be used for elasticity imaging.

In conclusion, a new class of iron oxide-gold core-shell NPs has been developed. In contrast to prior arts in which gold shells are deposited directly on iron oxide or iron oxide-silica composites, the core and shell of our particles are spatially separated with a dielectric polymer layer. This method allows formation of uniform MNP-gold particles *simultaneously* being compact in size and responsive in the NIR spectrum, which have not been achieved previously. The resulting NPs show highly integrated properties including electronic, magnetic, optical, acoustic, and thermal responses, which allow multimodality imaging. Beyond conventional NP based imaging modalities such as TEM, optical imaging, MRI, and PA, coupling of magnetic motion with photothermal conversion enables mmPA, a new modality with remarkable contrast enhancement compared to conventional PA imaging. We envision that the gold surface will also allow simple conjugation with biomolecular targeting ligands to develop all-in-one nanostructures for non-invasive imaging, molecular diagnosis, and hyperthermia-based treatment of complex diseases.

Methods

Chemicals and instruments

Unless specified, chemicals were purchased from Sigma-Aldrich (St. Louis, MO) and used without further purification. Oleic acid-capped monodisperse superparamagnetic iron oxide nanocrystals of different sizes were a gift from Oceannanotech LLC. PL-PEG-COOH (DSPE-PEG_{2000} carboxylic acid) was purchased from Avanti polar lipids (Alabaster, AL). PLH (MW ≥ 5,000) was used as the templates to direct gold nucleation and growth. A UV-2450 spectrophotometer (Shimadzu, Columbia, MD) was used to characterize NP absorption spectra. A tabletop ultracentrifuge (Beckman TL120) was used for NP purification and isolation. Particle size was measured on a CM100 transmission electron microscope (Philips EO, Netherlands). Dark field images were obtained on an IX-71 inverted microscope (Olympus, San Diego, CA) equipped with a Q-color5 digital color camera (Olympus). SQUID magnetometry was measured at 300K on a Quantum Design MPMS-5S SQUID Magnetometer (Quantum Design, San Diego, CA).

Solubilization of MNPs with PL-PEG-COOH

Oleic acid coated MNPs (1 mg) and PL-PEG-COOH (1.4 mg) were mixed in chloroform (1ml) followed by slow evaporation of the solvent. The residual solid was heated to 80 °C for 5 min to completely removed chloroform. The MNPs became soluble after adding deionized (DI) water (1 ml) and brief sonication. Excess lipids were purified out from the solubilized MNPs with repeated ultracentrifugation (25,000 rpm for 1h X 3 times). The purified MNPs were redispersed in 4 mL of DI water, to which 1.1 mg of PLH was added. The pH of the solution was adjusted to 5–6 using 0.1 N HCl. After incubation of 60 min, MNPs coated with PLH were again purified with ultracentrifugation and dispersed in 5 mL DI water.

Gold nanoshell growth

890 μl of DI water and 10 μl of $HAuCl_4$ (w/w 1%) aqueous solution (pH adjusted to 9–10 with NaOH) were added to 100 μl of the MNP-PLH solution, and incubated for 20 min. A reducing agent NH_2OH (20 mM, 20 μl) was then introduced to initiate the surface-confined Au shell growth. Upon mixing, the colloidal solution changed color from brownish-black to dark blue over a few minutes, indicating formation of gold nanoshells. The resultant gold shells are typically ~ 2–3 nm in thickness, which can be facilely tuned by changing the amount of gold ions. After synthesis, PEG-SH was used to enhance the colloidal stability.

Photoacoustic imaging

Particle samples were injected into a polycarbonate tube (CTPC167-200-5, Paradigm Optics, Vancouver, WA; 167 and 200 μm inner and outer diameters, respectively). A frequency doubled YAG pulsed laser (Surelite I-20, Continuum, Santa Clara, CA) with 5-ns pulse width pumped an optical parametric oscillator (Surelite OPO Plus, Continuum) to illuminate the tube at 750 nm wavelength and 3.3 mJ/cm^2 fluence. PA signals were received by the central 32 elements of an ultrasound linear array (L 14-5/38, Ultrasonix, Burnaby, BC, Canada) and recorded by an ultrasound scanner (Sonix RP, Ultrasonix). A delay-and-sum beamforming algorithm was used for image reconstruction. For NP stability against laser irradiation, samples were subjected to 30-min continuous irradiation at wavelengths close to the SPR peaks of each particle sample at fixed laser fluence.

Magnetomotive photoacoustic imaging

A phantom of 10% polyvinyl alcohol (PVA) disk with 3-mm thickness was constructed using three short freeze-thaw cycles. Three 2-mm diameter cylindrical inclusions made of 10% PVA mixed with 8% 15-um polymer beads (Bangs Laboratories, Inc., Fishers, IN) were placed within the phantom: the first one contained gold nanorods with about the same absorption coefficient as 3 nM MNP-gold hybrid NPs, the second contained 3 nM MNP-gold hybrid NPs, and the third contained 3 nM MNPs. An electromagnet integrated with a DC power amplifier, a current amplifier, and a function generator (Agilent 33250A, Santa Clara, CA), producing 5-s 0.7-Tesla pulses, was placed under a water tank holding the phantom. A frequency doubled YAG pulsed laser (Surelite I-20, Continuum, Santa Clara, CA) with 5-ns pulse width pumped an optical parametric oscillator (Surelite OPO Plus, Continuum) to illuminate the PVA phantom at 720 nm wavelength and 2.3 mJ/cm^2 fluence. A 15-MHz single element transducer (Olympus, Waltham, MA) was translated to scan 1D PA images. The RF signal was acquired using an amplifier (AM-1300, MITEQ, Hauppauge, NY) and a digital oscilloscope (LeCroy, Chestnut Ridge, NY).

MR imaging

Samples were scanned with a 3.0T whole body MRI scanner (Achieva, Philips Healthcare) using a phased array wrist coil. MR images were obtained using a 2D multi-slice-multi-echo spin echo (SE) sequence with various echo times. The imaging parameters were as following: repetition time, 2500 ms; echo times, 10/30/50/70/100 ms; field of view, 10 cm; matrix, 256×256; and thickness, 2 mm.

Supplementary Material

Refer to Web version on PubMed Central for supplementary material.

Acknowledgments

This work was supported in part by NIH (R01 CA131797, R01CA140295 to X.H.G), NSF (0645080 to X.H.G.), and the Department of Bioengineering at the University of Washington. X.H.G. thanks the NSF for a Faculty Early Career Development award (CAREER) and M.O.D. thanks the University of Washington for partial support of this work. We are also grateful to Dr. B.S. Qiu at UW Radiology for help with MRI, and X. Zhang for help with computer graphics.

References

1. Michalet X, et al. Quantum dots for live cells, in vivo imaging, and diagnostics. Science. 2005; 307:538–544. [PubMed: 15681376]
2. Murray CB, Kagan CR, Bawendi MG. Synthesis and characterization of monodisperse nanocrystals and close-packed nanocrystal assemblies. Ann. Rev. Mater. Sci. 2000; 30:545–610.

3. Niemeyer CM. Nanoparticles, proteins, and nucleic acids: Biotechnology meets materials science. Angew. Chem. Int. Ed. 2001; 40:4128–4158.
4. Kobayashi H, et al. Multimodal Nanoprobes for Radionuclide and Five-Color Near-Infrared Optical Lymphatic Imaging. ACS Nano. 2007; 1:258–264. [PubMed: 19079788]
5. Baker M. Whole-animal imaging: The whole picture. Nature. 2010; 463:977–980. [PubMed: 20164931]
6. Weissleder R. Scaling down imaging: Molecular mapping of cancer in mice. Nature Reviews Cancer. 2002; 2:11–18.
7. Jain PK, El-Sayed IH, El-Sayed MA. Au nanoparticles target cancer. Nano Today. 2007; 2:18–29.
8. Cheon J, Lee JH. Synergistically Integrated Nanoparticles as Multimodal Probes for Nanobiotechnology. Acc. Chem. Res. 2008; 41:1630–1640. [PubMed: 18698851]
9. Jeong U, Teng XW, Wang Y, Yang H, Xia YN. Superparamagnetic colloids: Controlled synthesis and niche applications. Adv. Mater. 2007; 19:33–60.
10. Lim J, Tilton RD, Eggeman A, Majetich SA. Design and synthesis of plasmonic magnetic nanoparticles. J. Magn. Magn. Mater. 2007; 311:78–83.
11. Goon IY, et al. Fabrication and Dispersion of Gold-Shell-Protected Magnetite Nanoparticles: Systematic Control Using Polyethyleneimine. Chem. Mater. 2009; 21:673–681.
12. Wang H, Brandl DW, Le F, Nordlander P, Halas NJ. Nanorice: A hybrid plasmonic nanostructure. Nano Letters. 2006; 6:827–832. [PubMed: 16608292]
13. Levin CS, et al. Magnetic-plasmonic core-shell nanoparticles. ACS Nano. 2009; 3:1379–1388. [PubMed: 19441794]
14. Wang LY, Bai JW, Li YJ, Huang Y. Multifunctional nanoparticles displaying magnetization and near-IR absorption. Angew. Chem. Int. Ed. 2008; 47:2439–2442.
15. Cho S-J, et al. Growth mechanisms and oxidation resistance of gold-coated iron nanoparticles. Chem. Mater. 2005; 17:3181–3186.
16. Lyon JL, Fleming DA, Stone MB, Schiffer P, Williams ME. Synthesis of Fe Oxide core/Au shell nanoparticles by iterative hydroxylamine seeding. Nano Letters. 2004; 4:719–723.
17. Xu Z, Hou Y, Sun S. Magnetic core/shell Fe3O4/Au and Fe3O4/Au/Ag nanoparticles with tunable plasmonic properties. J. Am. Chem. Soc. 2007; 129:8698–8699. [PubMed: 17590000]
18. Wang LY, et al. Monodispersed core-shell Fe3O4@Au nanoparticles. J. Phys. Chem. B. 2005; 109:21593–21601. [PubMed: 16853803]
19. Ji XJ, et al. Bifunctional gold nanoshells with a superparamagnetic iron oxide-silica core suitable for both MR imaging and photothermal therapy. J. Phys. Chem. C. 2007; 111:6245–6251.
20. Salgueirino-Maceira V, et al. Bifunctional gold-coated magnetic silica spheres. Chem. Mater. 2006; 18:2701–2706.
21. Kim J, et al. Designed fabrication of multifunctional magnetic gold nanoshells and their application to magnetic resonance imaging and photothermal therapy. Angew. Chem. Int. Ed. 2006; 45:7754–7758.
22. Jin Y, Gao X. Plasmonic fluorescent quantum dots. Nat. Nanotechnol. 2009; 4:571–576. [PubMed: 19734929]
23. Oldenburg SJ, Averitt RD, Westcott SL, Halas NJ. Nanoengineering of optical resonances. Chem. Phys. Lett. 1998; 288:243–247.
24. Lu X, Yavuz MS, Tuan H-Y, Korgel BA, Xia Y. Ultrathin gold nanowires can be obtained by reducing polymeric strands of oleylamine-AuCl complexes formed via aurophilic interaction. J. Am. Chem. Soc. 2008; 130:8900–8901. [PubMed: 18540574]
25. Cho SJ, et al. Growth mechanisms and oxidation resistance of gold-coated iron nanoparticles. Chem. Mater. 2005; 17:3181–3186.
26. Zhang J, Tang Y, Lee K, Ouyang M. Nonepitaxial growth of hybrid core-shell nanostructures with large lattice mismatches. Science. 327:1634–1638. [PubMed: 20339071]
27. Prodan E, Nordlander P, Halas NJ. Effects of dielectric screening on the optical properties of metallic nanoshells. Chem. Phys. Lett. 2003; 368:94–101.
28. Prodan E, Nordlander P, Halas NJ. Electronic Structure and optical properties of gold nanoshells. Nano Letters. 2003; 3:1411–1415.

29. Westcott SL, Jackson JB, Radloff C, Halas NJ. Relative contributions to the plasmon line shape of metal nanoshells. Phys. Rev. B. 2002; 66:155431.
30. Zhao W, Karp JM. Tumour targeting: Nanoantennas heat up. Nat. Mater. 2009; 8:453–454. [PubMed: 19458645]
31. Link S, El-Sayed MA. Spectral properties and relaxation dynamics of surface plasmon electronic oscillations in gold and silver nanodots and nanorods. J. Phys. Chem. B. 1999; 103:8410–8426.
32. El-Sayed MA. Some interesting properties of metals confined in time and nanometer space of different shapes. Acc. Chem. Res. 2001; 34:257–264. [PubMed: 11308299]
33. Jana NR, Gearheart L, Murphy CJ. Wet chemical synthesis of high aspect ratio cylindrical gold nanorods. J. Phys. Chem. B. 2001; 105:4065–4067.
34. Chen JY, et al. Immuno gold nanocages with tailored optical properties for targeted photothermal destruction of cancer cells. Nano Lett. 2007; 7:1318–1322. [PubMed: 17430005]
35. Chen JY, et al. Gold nanocages: Engineering their structure for biomedical applications. Adv. Mater. 2005; 17:2255–2261.
36. Hirsch LR, et al. Nanoshell-mediated near-infrared thermal therapy of tumors under magnetic resonance guidance. Proc. Nat. Acad. Sci. U.S.A. 2003; 100:13549–13554.
37. Song KH, Kim CH, Cobley CM, Xia YN, Wang LV. Near-infrared gold nanocages as a new class of tracers for photoacoustic sentinel lymph node mapping on a rat model. Nano Lett. 2009; 9:183–188. [PubMed: 19072058]
38. Yang XM, Skrabalak SE, Li ZY, Xia YN, Wang LHV. Photoacoustic tomography of a rat cerebral cortex in vivo with au nanocages as an optical contrast agent. Nano Lett. 2007; 7:3798–3802. [PubMed: 18020475]
39. Emelianov SY, Li PC, O'Donnell M. Photoacoustics for molecular imaging and therapy. Phys. Today. 2009; 62:34–39. [PubMed: 20523758]
40. Lubinski MA, Emelianov SY, O'Donnell M. Speckle tracking methods for ultrasonic elasticity imaging using short-time correlation. IEEE Trans. Ultrason. Ferroelectr. Freq. Control. 1999; 46:82–96. [PubMed: 18238401]
41. Fahey BJ, Hsu SJ, Trahey GE. A novel motion compensation algorithm for acoustic radiation force elastography. IEEE Trans. Ultrason. Ferroelectr. Freq. Control. 2008; 55:1095–1111. [PubMed: 18519218]
42. Shi Y, de Ana FJ, Chetcuti SJ, O'Donnell M. Motion artifact reduction for IVUS-based thermal strain imaging. IEEE Trans. Ultrason. Ferroelectr. Freq. Control. 2005; 52:1312–1319. [PubMed: 16245600]
43. Wang X, et al. Noninvasive laser-induced photoacoustic tomography for structural and functional in vivo imaging of the brain. Nat. Biotechnol. 2003; 21:803–806. [PubMed: 12808463]

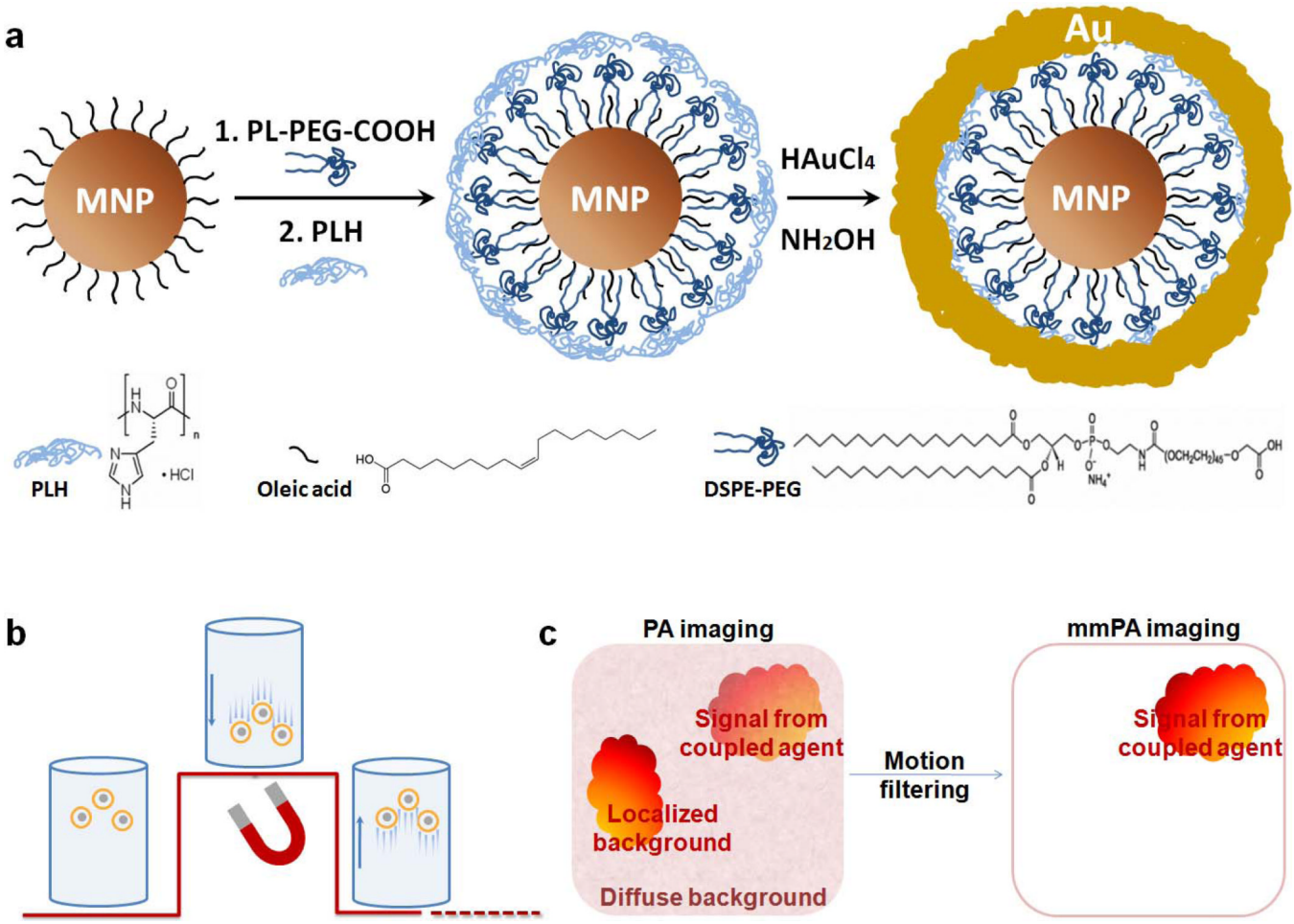

Figure 1. Schematic of MNP-gold core-shell NPs and mechanism of background suppression using mmPA

(a) Key steps involved in hybrid NP synthesis (figure not drawn to scale). Monodisperse hydrophobic MNPs coated with oleic acids are first solubilized using amphiphilic PL-PEG-COOH. PLH, which is capable of chelating metal ions, is then adsorbed onto PL-PEG-COOH via electrostatic interaction. Upon addition of gold ions and a reducing reagent, thin gold shells form on the polypeptide template rather than directly on the core nanoparticles. The molecular structures of oleic acid, PL-PEG-COOH, and PLH are shown below the reaction scheme. (b) Schematic of MNP-gold core-shell NPs' response to a magnetic field. The underlying red curve represents field strength. The coupled agents vibrate as the magnetic field is turned on and off. (c) Schematic of contrast enhancement in mmPA imaging. mmPA imaging suppresses regions not susceptible to a controlled magnetic field while identifying regions with coupled agents responsive to a magnetic field.

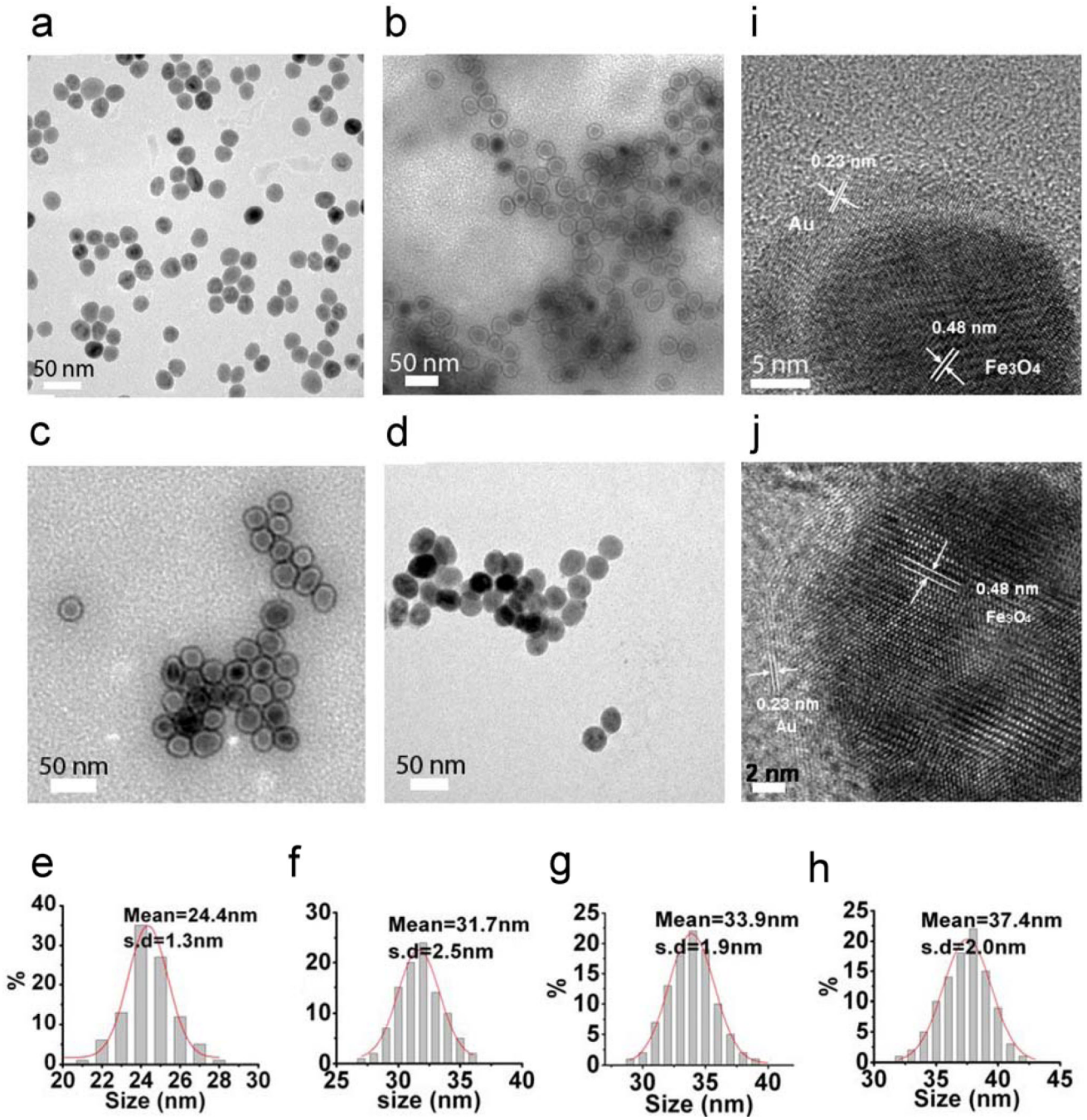

Figure 2. TEM imaging of the MNP-gold coupled agents

(a–d) TEM images and (a1–d1) size distribution histograms of (a) PL-PEG-COOH / PLH coated MNPs (polymer layer not visible under TEM due to low electron density), and (b–d) MNP-gold core-shell NPs with various shell thickness (b, ~1–2 nm; c, 2–3 nm; d, 4–5 nm). The particle size histograms in a1–d1 are plotted from analysis of > 150 particles for each sample. (e&f) Representative HR-TEM images of MNP-gold core-shell NPs with shell thickness of ~ 2–3 nm. The lattice spacing of the MNP core measures at 0.48 nm corresponding to the (111) plane of Fe_3O_4; whereas the (111) plane of face-centered cubic (fcc) Au shows 0.23 nm lattice spacing.

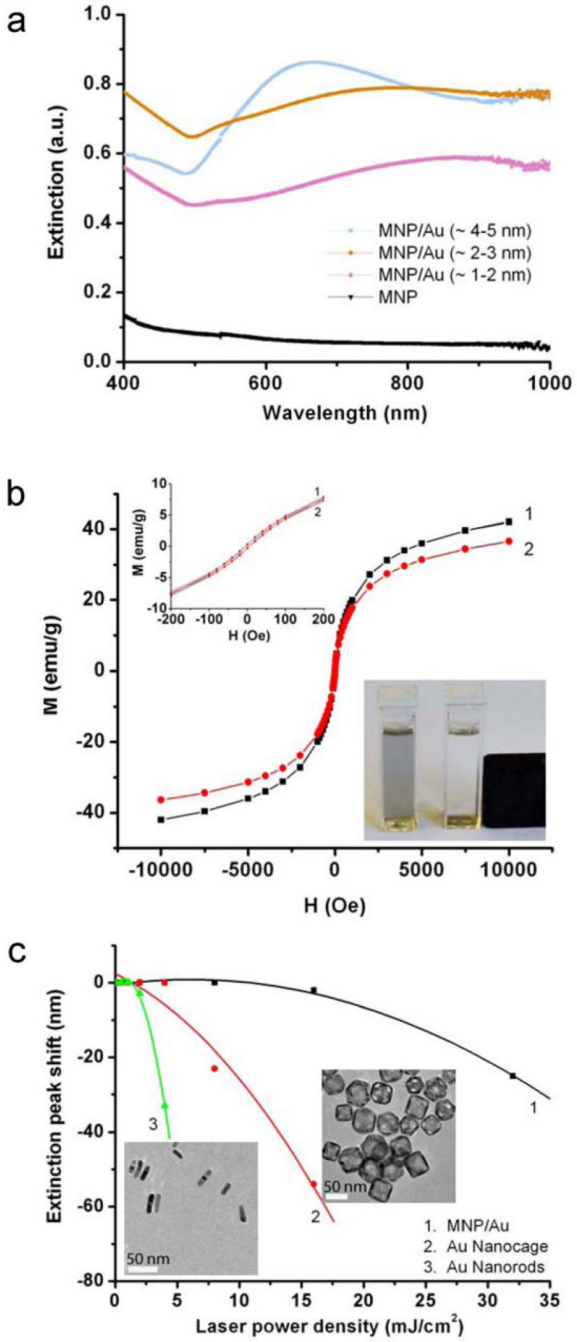

Figure 3. Optical and magnetic properties and stability of the MNP-gold hybrid NPs

(a) Extinction spectra of MNPs successively coated with PL-PEG-COOH and PLH (black), and with gold nanoshells of various thickness, 1–2 nm (brown), 2–3 nm (purple), and 4–5 nm (red). As the gold nanoshell thickness increases, the spectral intensity increases and the peak center blue shifts. (b) Magnetization as a function of magnetic field at room temperature for MNP (black) and MNP-gold (2–3 nm shell thickness) (red). The gold shell coating has negligible effect on MNPs' magnetic behavior. The insets show the absence of magnetic hysteresis and magnetic separation of the MNP-gold NPs. (c) Photothermal stability of the MNP-gold NPs in comparison with gold nanocages and nanorods. Extinction peak shifts as a function of laser fluence indicate that nanocages and nanorods start to

quickly degrade at 5 mJ/cm^2, whereas the MNP-gold hybrid NPs remain stable against laser irradiation of approximately three times higher fluence. TEM images of the nanocages and nanorods are shown as insets, scale bars are 50 and 100 nm for nanocages and nanorods, respectively.

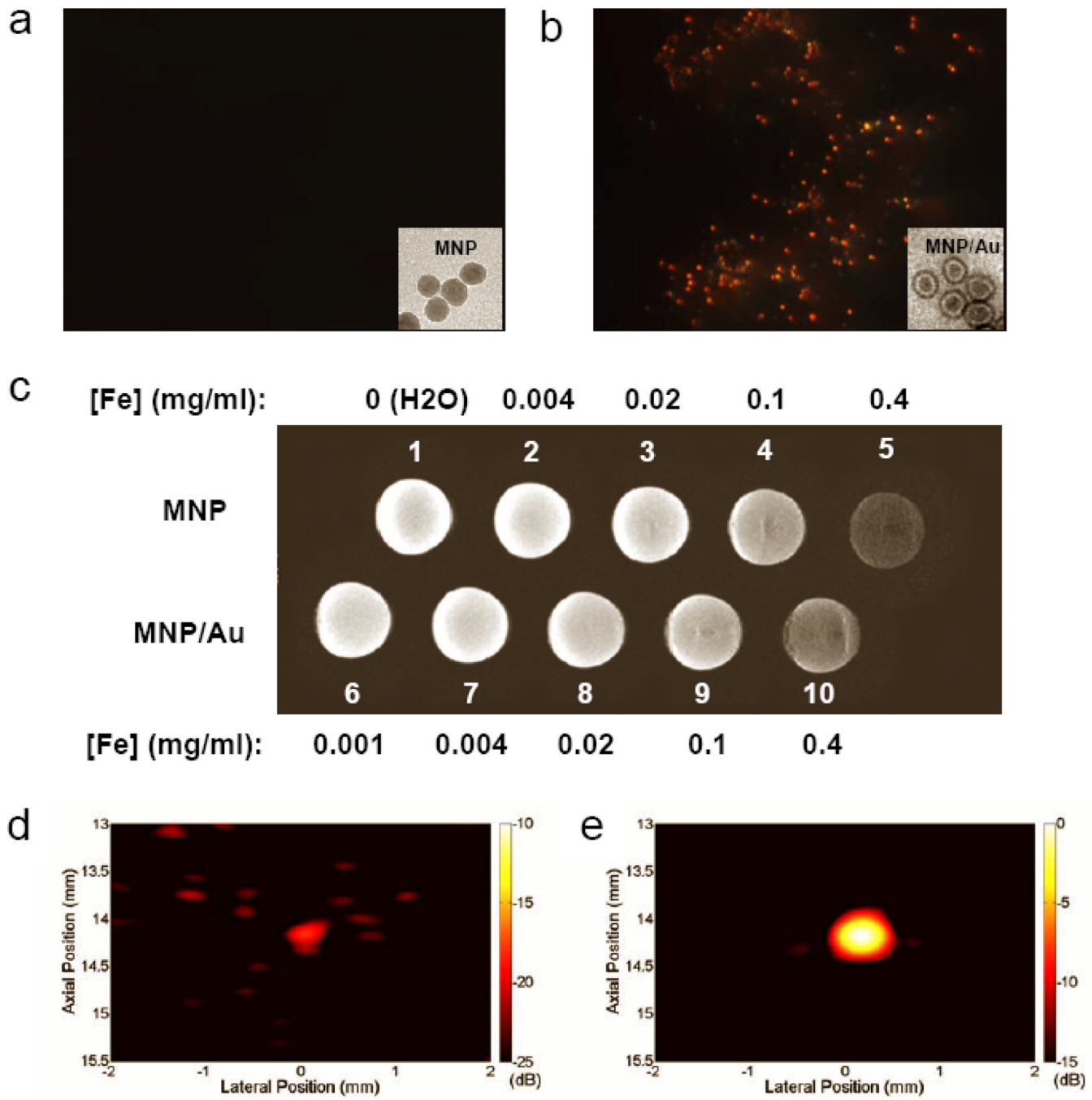

Figure 4. Multimodality imaging using the MNP-gold hybrid NPs

(a&b) Dark-field imaging of single MNPs spread on glass coverslips before and after gold nanoshell coating. The coated MNPs are readily detectable under current experiment conditions (insets show corresponding TEM images). (c) T2-weighted MR images of the bare and gold-coated MNPs at various dilutions. The signal strength is indicated by the darkness of the images. At the same concentrations, the MR images are indistinguishable between the two series indicating unchanged magnetic properties before and after gold nanoshell coating. (d&e) Cross-sectional PA images of a tube filled with (d) 5 nM MNPs and (e) 5 nM MNP-gold NPs on a dB scale. 0 dB corresponds to the maximum signal level among both images. Note that a different dynamic range was used for better visualization.

Signal-to-noise ratio can be improved by 1 order of magnitude (20 dB) when MNP-gold NPs are used.

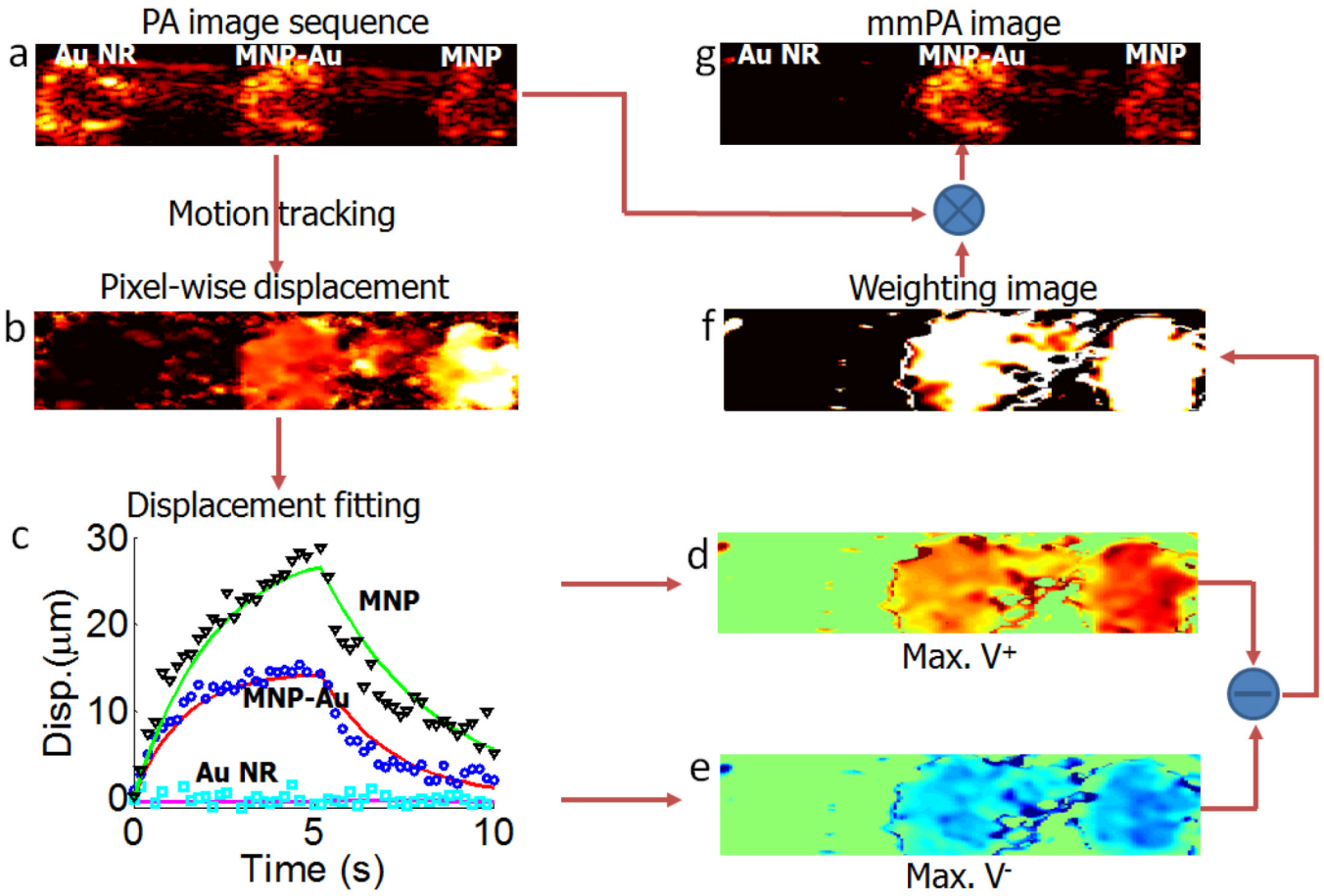

Figure 5. Data processing in mmPA imaging of MNP-gold hybrid NPs in comparison with gold nanorods and MNPs

A conventional PA image (a) sequence was acquired in synchrony with a magnetic pulse. (b) The maximum displacement achieved at the end of the magnetic pulse tracked using this sequence with the magnetic pulse spanning the first 5 seconds. (c) Three representative displacement courses and their fitted curves for pixels in different inclusions. The maximum positive (d) and maximum negative (e) velocities were derived from fitted displacement curves, and used to create a weighting image (f). The product of (a) and (f) produced an mmPA image (g), where the gold nanorod inclusion is completely suppressed. The display ranges are 40 dB dynamic range in (a) and (g), [0 (dark), 30 (light)] μm in (b), [−20, 20] μm/s in (d) and (e) with −20 μm/s, 0 μm/s, and 20 μm/s corresponding to dark blue, green, and dark red, respectively, and [0, 1] in (f).